

A Parameterized ASCAT Measurement Spatial Response Function

Richard D. Lindsley, *Member, IEEE*, Craig Anderson, Julia Figa-Saldaña, and David G. Long, *Fellow, IEEE*

Abstract—The Advanced SCATterometer (ASCAT) measurement spatial response function (SRF) relates the weighted contribution of every location within the measurement footprint to the measured normalized radar cross section σ° . The SRF results from a combination of the antenna response and the onboard processing and is computed during ground processing by modeling in detail the measurement geometry, as this is required for an accurate σ° estimation. However, the computed SRF is not disseminated as part of the L1B data. For some applications of the L1B data, the SRF is additionally required. For these applications, an approximate description of the SRF is often sufficiently accurate, estimated from information contained in the L1B data, rather than from a full calculation based on the measurement geometry. This paper describes a parameterized model of the ASCAT SRF for each measurement. First, an SRF reference estimate that incorporates details on the ASCAT design and onboard measurement processing is created. A parameterized model is fit to the reference estimate. The parameterized SRF is computationally less demanding than the reference estimate and as such more useful for near-real-time processing. The two estimates are validated with the computed SRF used in ground processing and with the transponder data from calibration campaigns. Finally, to validate the SRF in a simple application, the land fraction (a measure of land contamination in near-coastal ocean measurements) is computed and compared to actual data for a sample region.

Index Terms—Advanced SCATterometer (ASCAT), radar measurements, radar remote sensing, scatterometer, spaceborne radar.

I. INTRODUCTION

THE Advanced SCATterometer (ASCAT) on the MetOp series of satellites has proven useful in a variety of geoscience applications. In addition to the primary mission to retrieve ocean vector winds from radar backscatter measurements, ASCAT data have been used for mapping sea ice and oil spills [1], tracking icebergs, and measuring soil moisture content [2], among other land and ocean climate studies [3].

Each ASCAT measurement of radar backscatter, or σ° , has an associated spatial response function (SRF). The measurement

SRF dictates the weighted contribution of the area of the Earth's surface around the measurement center. While the σ° measurement alone is useful, some applications additionally require a good knowledge of the SRF associated with each measurement. One such application is coastal scatterometry, where an accurate knowledge of the fraction of land contributing to a radar response is necessary. The land fraction, also termed the land contribution ratio (LCR), is a metric for how much land contamination is present in an ASCAT measurement over the ocean. This may be used to objectively keep or discard near-coastal ocean measurements of radar backscatter, enabling near-coastal wind retrieval.

The ASCAT ground Product Processing Facility (PPF) uses the integrated measurement SRF to create level 1B data. Although the PPF may output the SRF for test purposes, the SRF is not included in the published L1B product. We develop an estimate of the measurement SRF that employs as inputs quantities reported in the L1B data. To reduce the computational demands of the estimate, the SRF may be parameterized.

In this paper, we derive a parameterized estimate of the ASCAT SRF and demonstrate its utility by comparing the measurement land fraction to σ° measurements. Section II contains background information on ASCAT as well as the SRF. Section III describes the various components that shape the SRF. This serves as a reference estimate used to create the parameterized approximation in Section IV. The two estimates are validated in Section V. As an application of the SRF, the land fraction is shown in Section VI. Section VII concludes this paper.

II. BACKGROUND

ASCAT is a fan beam scatterometer operating at 5.255 GHz (C-band) with vertical polarization [4]. The ground geometry is illustrated in Fig. 1. Six beams (three for each of the two swaths) measure at fore, mid, and aft azimuth angles. Range-gate dechirping subdivides each fan beam into 256 measurements at varying incidence angles, although only a subset of 192 measurements is reported in the current L1B format. The measurement node number indexes the measurements along each beam. As the node number increases, so do the incidence angle, slant range, and ground range. The six beams are periodically calibrated to maintain the accuracy of the σ° measurements and the derived geophysical parameters, such as wind or soil moisture.

An ASCAT instrument currently operates on each of the MetOp-A and MetOp-B satellites, launched in 2006 and 2012, respectively. This paper only considers data from the MetOp-A

Manuscript received June 18, 2015; revised February 13, 2016; accepted March 15, 2016. Date of publication April 11, 2016; date of current version June 1, 2016.

R. D. Lindsley was with the Microwave Earth Remote Sensing Laboratory, Brigham Young University, Provo, UT 84602 USA. He is now with Remote Sensing Systems, Santa Rosa, CA 95401 USA (e-mail: lindsley@remss.com).

C. Anderson and J. Figa-Saldaña are with the European Organisation for the Exploitation of Meteorological Satellites (EUMETSAT), 64295 Darmstadt, Germany (e-mail: craig.anderson@eumetsat.int; julia.figa@eumetsat.int).

D. G. Long is with the Department of Electrical and Computer Engineering and the Microwave Earth Remote Sensing Laboratory, Brigham Young University, Provo, UT 84602 USA (e-mail: long@ee.byu.edu).

Color versions of one or more of the figures in this paper are available online at <http://ieeexplore.ieee.org>.

Digital Object Identifier 10.1109/TGRS.2016.2544835

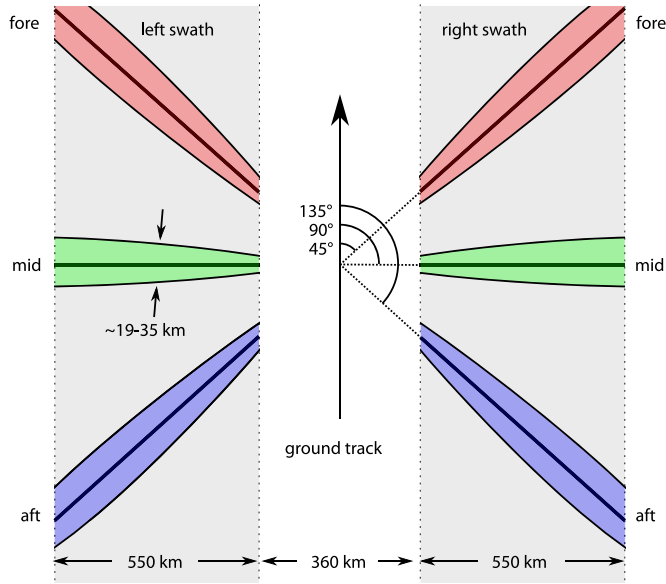


Fig. 1. ASCAT ground measurement and swath geometry. Each swath is sampled at a range of incidence angles at fore, mid, and aft azimuth angles. Surface beamwidth is exaggerated for illustrative purposes.

ASCAT, although the results are similar for the MetOp-B ASCAT. The MetOp satellites are in a sun-synchronous near-polar orbit with a ground track repeat of 29 days [4].

ASCAT samples the Earth surface σ° over a distributed area filtered with an aperture function. Neglecting measurement noise, a model for the reported backscatter measurement produced by ASCAT is of the form

$$s_i = \iint \sigma^\circ(x, y) h_i(x, y) dx dy \quad (1)$$

where measurement s_i is the weighted combination of the surface normalized radar cross section (NRCS) and the SRF $h_i(x, y)$ for measurement i [5]. The index subscript i has an arbitrary range and is included since the SRF is not identical for all measurements, but each measurement s_i has an associated unique SRF $h_i(x, y)$ that differs from the SRFs for other measurements. The SRF represents the contribution from each location within the ground footprint and is a variable aperture function—i.e., the aperture function for each measurement may differ due to sampling geometry. The x and y variables represent location. For convenience, a locally tangent plane convention [6] is adopted with the SRF estimates described in this paper. For each measurement i , a different plane is used, tangent to the Earth at the reported measurement center. Operating in the tangent plane permits working in units of linear distance (e.g., kilometers) from the measurement center rather than in latitude and longitude. Because the tangent plane is aligned with north, the axes are in northing and easting.

The measurement values (radar backscatter, incidence angle, and azimuth angle) and location (in latitude and longitude) are reported for each measurement within each beam. This is the “full resolution” (SZF) L1B product. Spatially averaged products are also produced, in which a swath-oriented grid is defined and the value at each grid point is the combination of all

TABLE I
PARAMETERS FOR A SAMPLE ASCAT MEASUREMENT USED FOR FIG. 3

Beam	Right mid
Pass	Ascending
Incidence angle	38.24°
Range bin number	100
Location	66.52°N 299.67°E
Date	2011-10-26 (DOY 299)
Time	1:00:01.254Z

nearby full-resolution measurements, spatially weighted with a Hamming window. This paper does not consider the spatially averaged products.

The SRF is used to define the land fraction, also termed the LCR [7]. The land fraction is a measure of the amount of land in a measurement over the ocean. This is a useful metric to assist in near-coastal wind retrieval: before retrieving the wind from the σ° measurements, the measurements may be kept or excluded based on exceeding a determined land fraction threshold.

The LCR is defined as

$$\text{LCR}_i = \frac{\iint L(x, y) h_i(x, y) dx dy}{\iint h_i(x, y) dx dy} \quad (2)$$

where i indexes the measurements, $L(x, y)$ is a binary-valued land indicator function, and $h_i(x, y)$ is the SRF for measurement i [7]. Using the locally tangent plane, x and y are the distance in easting and northing from the measurement center. In practice, the land map and SRF values are discretized

$$\text{LCR}_i = \frac{\sum_{x, y} L[x, y] h_i[x, y]}{\sum_{x, y} h_i[x, y]} \quad (3)$$

Due to the normalization, the land fraction varies between 0 and 1, where 0 is open ocean unaffected by land and 1 is entirely over land. Assuming that σ° is spatially homogeneous over the land and over the ocean portions of the footprint, the measurement value from (1) may be decomposed into

$$s_i = \sigma_{\text{land}}^\circ \text{LCR}_i + \sigma_{\text{ocean}}^\circ (1 - \text{LCR}_i) \quad (4)$$

where the measurement is a convex combination of the ocean and land σ° values, weighted by the LCR [7].

III. ASCAT SRF

The measurement SRF is modeled as the combination of several factors. The three main components examined here are the following: 1) the antenna beam response; 2) the frequency response of the FFT-based onboard processing; and 3) the along-track pulse averaging performed onboard. Other factors may also influence the SRF, such as the onboard receive filter response, but these do not influence the response to the same extent as those outlined in the following. In the following sections, the SRF components are progressively illustrated in Fig. 3 using a sample measurement with parameters listed in Table I.

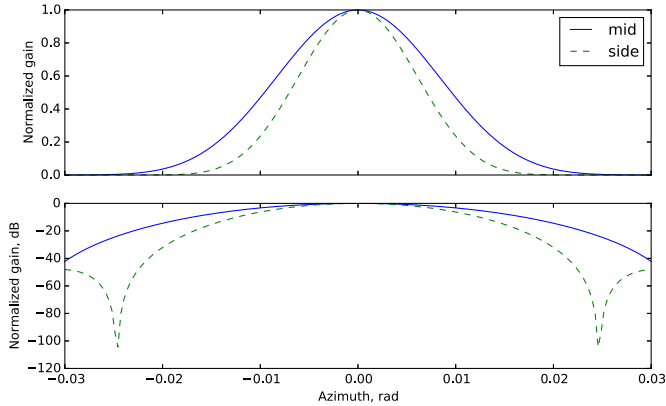


Fig. 2. Cross-beam or azimuthal nominal antenna patterns. The mid (solid) and side (dashed) beams are shown together. The upper subplot is in linear space, and the lower subplot is in dB space. The values shown are for the magnitude-squared normalized antenna gain pattern.

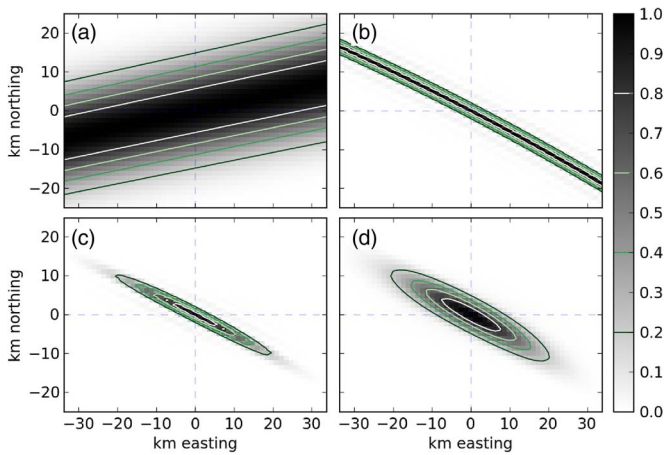


Fig. 3. SRF is progressively built up by including various components: (a) the cross-beam antenna response, (b) the range-gate response for a single FFT bin, (c) the pulse SRF, and (d) the full SRF. The SRF shown is for the measurement with parameters given in Table I.

A. Antenna Beam Response

The first component to the SRF is the response resulting from the antenna beam pattern. Of the six ASCAT beams, the antenna patterns of the four side beams are essentially identical to each other, and the patterns for the two mid beams are likewise identical.

In the following, only the antenna patterns in the cross-beam (or azimuth) direction are used. While the antenna response varies along the length of the beam (or elevation), we consider the along-beam response to be constant for each individual measurement. Because the modeled SRF is normalized, this also normalizes out the bulk along-beam response.

To account for the use of the antenna response for both transmission and reception, the magnitude-square of the normalized antenna gain pattern is used. This is shown for the mid and side beams in Fig. 2.

The antenna response for the sample measurement (with parameters listed in Table I) is illustrated in Fig. 3(a). The response is computed on a plane tangent to the measurement center [8].

B. Range-Gate Dechirping

The second component to the SRF is the range-gate dechirping performed onboard. The range-gate dechirping subdivides the fan beam antenna response, providing range resolution.

ASCAT is a pulsed radar, with each pulse a linear frequency-modulated chirp. The received signal—a sum of time-delayed and attenuated copies of the transmit chirp—is dechirped to baseband. This baseband signal is termed the *discriminator signal* and is sampled at 412.5 kHz. The power spectrum of the discriminator signal is estimated using Welch's method (viz., Fourier transforms of multiple overlapping segments of the sampled time-domain data are computed separately, magnitude-squared, and then averaged together). The discretely sampled power spectrum is the received power as a function of *discriminator frequency* [4], [5], [9], denoted here as $P[f]$.

The center frequency of each discriminator frequency FFT bin is given by

$$f_{\text{offset}} - \underbrace{\frac{4\alpha s}{c}}_{f_r} - \underbrace{\frac{2v_r}{\lambda}}_{f_d} = m\delta_f \quad (5)$$

where f_{offset} is a beam-dependent frequency offset, α is half of the beam-dependent chirp rate, s is the slant range from ASCAT to the Earth surface, c is the speed of light in a vacuum, v_r is the radial velocity between ASCAT and the Earth surface, λ is the radar wavelength, m is the FFT bin number, and δ_f is the frequency bin width. The values for these parameters are given in [5] and [8]. As noted by the underbraces, the discriminator frequency has components due to a range frequency f_r and a Doppler frequency f_d . The received power is normalized to σ° using the radar equation, and (5) is solved for the slant range s , so $P[f]$ maps to $\sigma^\circ[s]$.

Due to the nature of the discrete Fourier transform, each FFT bin has an associated frequency response: the power in the bin is the weighted combination of signals at many frequencies. Since each (continuous) discriminator frequency in (5) maps to a point on the Earth surface, the bin frequency response maps to a spatial response on the ground.

To estimate the range-gate SRF component, a locally tangent plane is defined centered on the measurement. For each location (x, y) on the locally tangent plane, the discriminator frequency is computed, including the range and Doppler frequencies. This entails modeling the Earth surface as an ellipsoid, accounting for the rotation of the Earth, and modeling the instantaneous orbit velocity; further details on this computation may be found in [8]. The frequency response of the 512-point onboard FFT, including the window function, is used to compute the FFT-induced ground response. The spatial response due to the FFT is shown in Fig. 3(b) for the sample measurement of Fig. 3. In other words, this is the response for a single discriminator frequency range bin projected to the ground including accounting for the Doppler shift.

The cumulative effect of the range-gate dechirping on the antenna pattern is shown in Fig. 3(c), which is a multiplication of the two responses in Fig. 3(a) and (b). This is the SRF at a particular node for a single ASCAT pulse and so is termed the pulse SRF. Due to a nonnegligible Doppler frequency f_d ,

the pulse SRF is rotated by roughly 60° from the cross-beam direction. We generally observe that the shape of the pulse SRF, due to the rotation, is elliptical.

C. Along-Track Pulse Averaging

The final major component to the SRF is the along-track pulse averaging performed onboard ASCAT [9]. Each reported measurement is the weighted average of eight pulses. The weights are the following: $\{0.05, 0.10, 0.15, 0.20, 0.20, 0.15, 0.10, 0.05\}$, and a measurement is saved every four pulses. The radar itself has a pulse repetition frequency (PRF) of approximately 28.26 Hz [10]. This is divided among the six beams, which are pulsed in sequence (left fore, left mid, left aft, right fore, right mid, and right aft). Thus, the PRF for each beam is $28.26/6 = 4.71$ Hz. The measurements are stored at a PRF of $4.71/4 = 1.1775$ Hz or about every 5.6 km along-track.

The individual pulse locations are not reported in the LIB data so are estimated based on the measurement location, the along-track direction, and the ground-track velocity of about 6.7 km/s. The measurement SRF is computed by shifting the pulse SRFs to the correct locations and summing them together using the weighting given previously [8]. The resulting measurement SRF for the sample measurement is shown in Fig. 3(d). We generally observe that pulse averaging gives the measurement SRF a more elliptical shape.

IV. PARAMETERIZED SRF

Although the SRF may be computed using the components outlined in Section III, it is time-consuming to process. In order to increase the utility of the SRF, we develop a parameterized variant. This both speeds up the processing and simplifies the code required to implement it.

The parameterization is based on the observation that the measurement SRF estimate is generally an ellipse, rotated such that the semiminor axis is aligned with the spatial gradient of the discriminator frequency. The discriminator frequency gradient is the direction in the tangent plane that the discriminator frequency as a function of location (x, y) varies most. The rotation angle between northing and the discriminator frequency gradient is termed ψ . The SRF is treated as separable in the directions aligned with the ellipse semimajor and semiminor axes. Three parameters are modeled: 1) the ellipse rotation angle ψ ; 2) the SRF response along the x (semiminor) axis; and 3) the SRF response along the y (semimajor) axis. To compute the SRF value for a location near a measurement, the following high-level algorithm is used.

- 1) Define a location on the locally tangent plane centered on the measurement.
- 2) Rotate from tangent plane coordinates (x_{tp}, y_{tp}) to coordinates with respect to the SRF ellipse (x_d, y_d) using the angle ψ .
- 3) Look up the SRF response in the x direction.
- 4) Look up the SRF response in the y direction.
- 5) Multiply the x and y response values together to obtain the SRF value.

TABLE II
ANGLES β AND φ FOR THE SIX ASCAT BEAMS. β IS THE ANGLE BETWEEN ALONG-BEAM AND ALONG-TRACK, AND φ IS THE ANGLE BETWEEN ALONG-TRACK AND NORTHING. THE ANGLE ϕ IS THE AZIMUTH ANGLE REPORTED IN THE LIB DATA

Beam	β	φ
1	45°	$\phi - 135^\circ$
2	90°	$\phi - 90^\circ$
3	135°	$\phi - 45^\circ$
4	-45°	$\phi + 135^\circ$
5	-90°	$\phi + 90^\circ$
6	-135°	$\phi + 45^\circ$

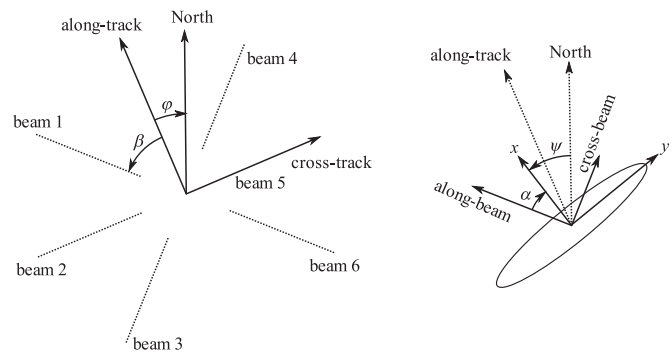


Fig. 4. (Left) Rotation angles φ and β for beam 1. (Right) Rotation angles α and ψ for beam 1.

The rotation angle ψ is a function of latitude. We decompose ψ into constituent angles

$$\psi = (-\varphi) + \beta + \alpha \quad (6)$$

where ψ is the angle from northing to the discriminator frequency gradient, φ is the rotation angle from along-track to northing, β is the rotation angle from along-track to along-beam, and α is the angle from along-beam to the discriminator frequency gradient (or, the x direction). The angles φ and β are functions of beam geometry and are defined in Table II. Fig. 4 illustrates the rotation angles discussed. The SRF ellipse semiminor axis x follows the discriminator frequency spatial gradient. In all cases, the angles are defined so that positive values are in the counterclockwise direction.

The angle ψ is obtained directly in the reference SRF estimate by computing the gradient of the computed discriminator frequencies on the tangent plane grid. At high latitudes, ψ rapidly varies due to φ , the angle between along-track and north. However, α is much more stable as a function of latitude, so it is parameterized rather than ψ . The remaining components of ψ — β and φ —are only a function of the beam number and azimuth angle so are not parameterized.

The angle α is due to the Doppler shift. If α were 0, then the SRFs would be aligned perpendicular to the beam. However, since the Doppler frequency in (5) is nonnegligible, the SRFs are rotated, as conceptually illustrated in Fig. 5. To first order, $\alpha \approx \pm 55^\circ$ but varies somewhat as a function of measurement node (i.e., incidence angle), latitude, and beam azimuth angle. An example is shown in Fig. 6. A fourth-order polynomial surface is fit individually for each of the

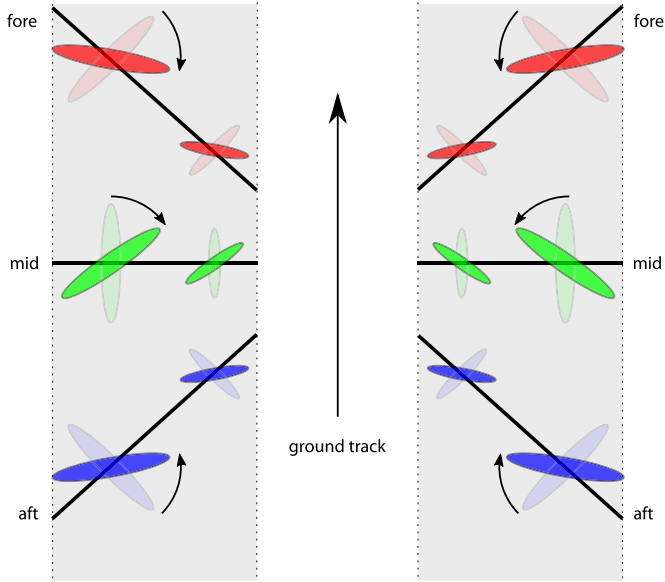


Fig. 5. Illustration of the impact of the rotation angle α on the SRFs. If Doppler shift were negligible, the rotation angle α would be zero, and the SRFs would lie perpendicular to the ASCAT beams. However, due to the Doppler frequency, $\alpha \approx \pm 55^\circ$, and therefore, the SRFs are rotated with respect to the beams.

six beams, separately for ascending and descending passes. The α parameterization is

$$\alpha(n, l; b, a) = c_{00} + c_{01}n + c_{02}n^2 + \dots + c_{10}l + c_{11}nl + \dots + c_{44}n^4l^4 \quad (7)$$

where n is the node number, l is the latitude, b is the beam number, and a is ascending or descending. For each combination of b and a , $(4 + 1)^2 = 25$ coefficients are required. With six beams ($b \in \{1, \dots, 6\}$) and two cases for ascending/descending ($a \in \{0, 1\}$), there are 12 sets of coefficients, or 300 total coefficients, to parameterize α . The coefficients are determined by computing the reference SRF estimate described in Section III for a large number of ASCAT measurements, randomly distributed in latitude and node. The angle α is computed for each measurement, and the data are fit in the least-squares sense to solve for the coefficients.

The SRF response values in the x and y directions may be modeled by a Gaussian fit. However, to reduce the model error while retaining a simple parameterization, we describe here a polynomial fit to the SRF response. A low-order polynomial fits the SRF mainlobe more closely in dB space than linear space. The polynomial fit is constrained, so it only fits the mainlobe down to -15 dB in order to avoid fitting the “ripples” in the mainlobe. A biquadratic fit is applied, or a fourth-order polynomial fit with the odd terms set to 0 to enforce symmetry

$$\text{SRF}_x(x; \dots) = a_0 + a_2x^2 + a_4x^4 \quad (8)$$

$$\text{SRF}_y(y; \dots) = b_0 + b_2y^2 + b_4y^4 \quad (9)$$

where x and y are in units of kilometers from the center of the locally tangent plane. A sample SRF response and the polynomial fit are shown in Fig. 7.

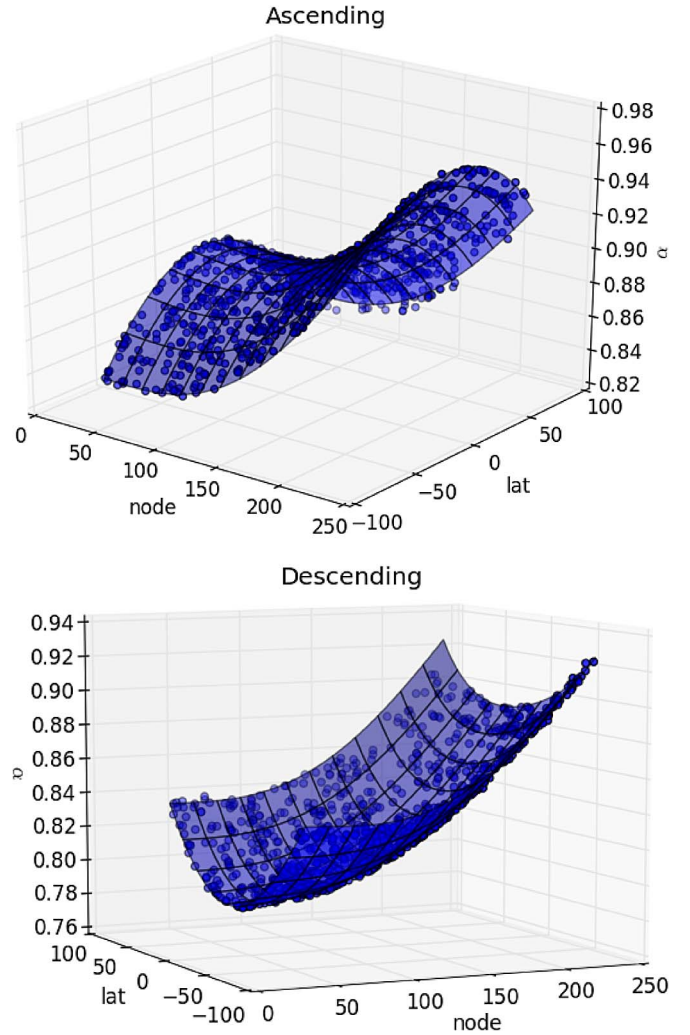


Fig. 6. Angle α , in radians, is shown as a function of node and latitude for the right aft beam for both ascending and descending passes. The points shown are a subset from five days of ASCAT data. The surface, a fourth-order polynomial described in the text, is fit to the points.

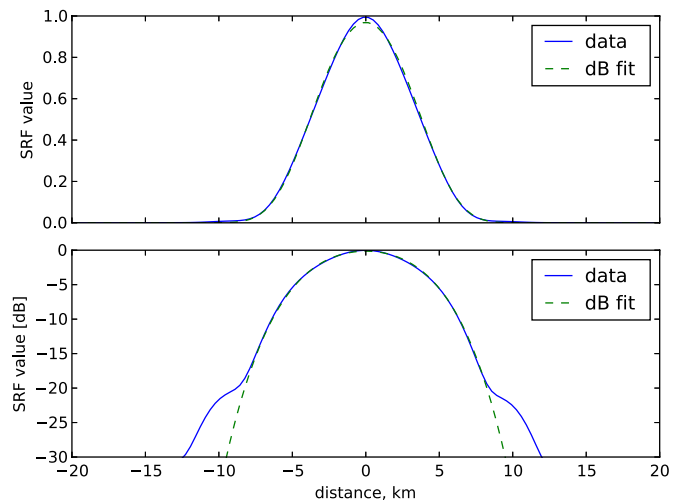


Fig. 7. SRF values along the x -axis for a measurement from beam 3. The upper subplot shows the values in linear space, and the lower subplot shows the values in dB space. A biquadratic fit in dB space is applied to the data down to -15 dB.

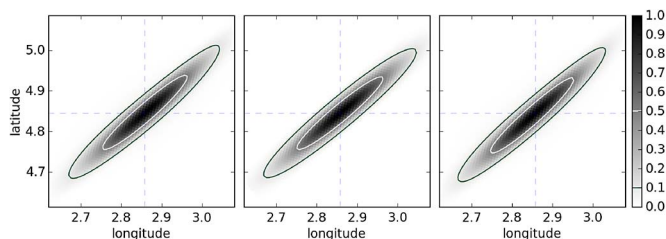


Fig. 8. Reference (left) and parameterized (center) SRF estimates and the PPF SRF (right) for a measurement in the left mid beam.

Equations (8) and (9) model the SRF response. The coefficients are, as with the angle α , functions of node, latitude, beam, and ascending/descending pass. A polynomial surface is fit to each coefficient as a function of node and latitude. However, unlike for α , only a second-order polynomial surface is required. For example, for the a_0 coefficient from (8)

$$a_0(n, l; b, a) = a_{00} + a_{01}n + a_{02}n^2 + a_{10}l + a_{11}nl + \dots + a_{22}n^2l^2. \quad (10)$$

For each of the six coefficients from (8) and (9), there are $(2 + 1)^2 = 9$ coefficients. As with α , the fits are separately performed by beam and ascending/descending pass for 12 cases. Thus, $6 \times 9 \times 12 = 648$ coefficients are used to parameterize the SRF response in the x and y directions.

The parameterized SRF is much less computationally demanding than the reference estimate from Section III. For example, the SRF is evaluated at 100 points around a measurement center using a consumer laptop from 2012. Using the reference SRF estimate, this computation completes in 20 ms; the parameterized SRF estimate, however, takes 0.10 ms to complete.

This decrease in runtime by two orders of magnitude does not appreciably affect the accuracy of the SRF estimate. Comparison plots for the reference and parameterized SRF estimates are shown in Fig. 8 for a mid beam. The SRF values are very similar for the reference and parameterized estimates. The largest differences are for those measurements with low incidence angles in the mid beams (not shown). In these cases, the reference SRF curves slightly, deviating from the ellipse model. Since the difference is small, and in the interest of a simple parameterization, the curvature is not accounted for.

Our parameterized SRF estimate is publicly available,¹ including the coefficients for the polynomial fits.

V. SRF VALIDATION

We validate the SRF estimates from Sections III and IV using several techniques. The first is a comparison with the SRF model used during the ground processing of the raw data from ASCAT. Second, we compare the SRF estimates against the spatial signal seen in the transponder data collected for the external calibration of ASCAT. Finally, we validate by examining the behavior of the ASCAT σ° data and showing that the

observed features are consistent with those predicted by the SRF estimates.

A. Ground Processing

If $\sigma^\circ(x, y)$ is constant over the area of the SRF, then the measured signal from (1) is related to σ° by

$$\sigma^\circ = \frac{s_i}{\iint h_i(x, y) dx dy}. \quad (11)$$

The integral acts as a normalization factor for converting the ASCAT measurement s_i into a calibrated NRCS.

The ASCAT antenna gain pattern is accurately determined through periodic calibration campaigns using several ground-based transponders. This, along with knowledge of the satellite position, enables the ASCAT processor to use numerical integration to calculate (11) and produce tables of normalization factors for converting ASCAT measurements into calibrated NRCS.

The ASCAT processor can be modified to output the SRF and the normalization factors for test purposes. Thus, a simple validation of the SRF estimate presented in this paper is a comparison against the SRF produced by the ASCAT ground processor at the PPF.

Example SRF values from the ASCAT processor are shown in Fig. 8 along with the SRF estimates discussed in this paper. Because the parameterized SRF is only designed to be accurate to -10 dB relative to the peak value, the SRF values are compared over a wide range with contours at -3 and -10 dB since this is the range of interest. We observe that they agree well, although they are not identical—some small error is expected due to approximations undertaken to create a simple model and parameterization of the SRF.

In all cases examined (SRFs calculated in near, mid, and far range in each beam), the two approaches produce similar results, and we conclude that the parameterized SRF is a good approximation for the SRF used by the ASCAT processor.

B. Transponder Data

We next validate the SRF by comparison against the transponder data used for external calibration. The ASCAT gain patterns are estimated using measurements of the signals from three transponders located in Turkey. When ASCAT approaches the transponders, it switches into calibration mode, in which the antenna beam passing over the region of transponders operates more frequently than in normal measurement mode.

The transponders track the satellite as it passes. When they detect the ASCAT signal, they wait for a fixed period and then transmit a copy of the signal back to the satellite. This time delay allows the transponder signal to reach ASCAT after the echos from the ground have died away, allowing the two to be clearly distinguished.

The magnitude of the transponder signal received by ASCAT depends on the position of the transponder in the beam pattern. The transponder data from each pass can be processed using the viewing geometry, the instrument characteristics, and the radar cross section of the transponder to produce a set of gain values on a line of points through the 2-D antenna beam pattern.

¹<http://www.scp.byu.edu/software/ASCAT>



Fig. 9. Example image of the ASCAT calibration mode data showing two transponders in the right three beams. For each beam, the horizontal axis is range (cross-track), and the vertical axis is time (along-track).

The locations of the three transponders are carefully chosen so that the antenna beam patterns are well sampled over the course of the MetOp repeat cycle. Given sufficient measurements, acquired over a period of one or two months, the complete 2-D antenna gain pattern can be reconstructed.

An example image showing the ASCAT data produced during calibration mode is given in Fig. 9, where the right three beams have passed over two transponders. The horizontal axis in each image corresponds to range, and the vertical axis corresponds to time (or along-track position). The images in the fore and aft beams are larger than in the mid beam as the calibration mode generally starts before the fore beam reaches the transponders and ends after the aft beam has passed over the transponders.

The transponders act as point targets; hence, the transponder signals seen in Fig. 9 should be direct measurements of the ASCAT SRF (although without along-track pulse averaging and with minor differences due to slightly different onboard processing in calibration mode). Thus, the transponder data may be used to estimate the SRF. We validate the modeled SRF by comparing it against the transponder-derived SRF.

We obtain an SRF from the transponder data by taking each along-track measurement over the transponder, deriving the corresponding antenna gain value, scaling the measurement so its peak value matches the gain value, and squaring (as the SRF is based on the two-way gain pattern rather than on the one-way gain pattern used in ASCAT calibration). The resulting 2-D function is then normalized to yield an estimate of the SRF. Fig. 10 shows the peak value of the resulting SRF as a function of along-track position compared to a model SRF produced by the ASCAT processor. There is a good agreement between the two, although we note that the transponder data are slightly noisy.

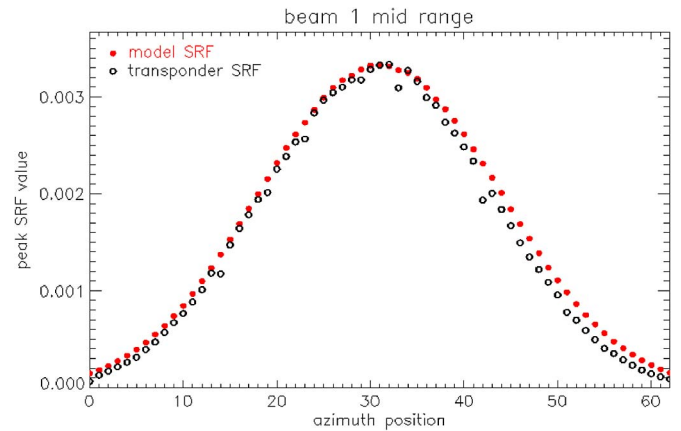


Fig. 10. As a slice through the along-track direction, a comparison of SRF values derived from transponder data against SRF values produced by the ASCAT processor.

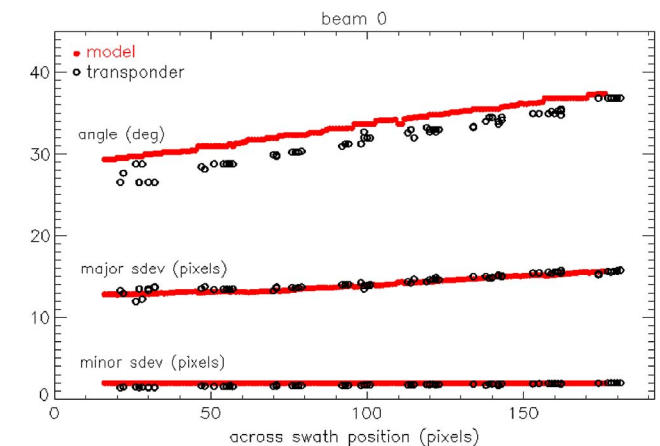


Fig. 11. Comparison of the parameters of Gaussian functions fitted to the SRF in beam 0 (left fore beam) derived from transponder data and from the model SRF produced by the ASCAT processor.

An ASCAT calibration campaign typically lasts two to three months, during which the satellite passes over the transponders around two times per day. The viewing geometry changes during the MetOp 29-day repeat cycle, and the transponders appear at different positions across the swath. For the set of transponder data acquired from September 2014 to January 2015, we obtain the set of measurement SRFs and fit rotated Gaussian functions to the SRFs. Gaussian functions, rather than the polynomial fit described in the previous section, are selected here to simplify the comparison of SRF parameters: a Gaussian fit is parameterized only by the orientation angle and the widths in the major and minor directions.

Fig. 11 shows the three parameters from the fitted Gaussians in the left fore beam and those of the model SRF. We find a good agreement between the two, although the orientation of the transponder SRF is consistently a few degrees less than that of the model.

The results for the left mid and aft beams (not shown) are similar to those of the fore beam, where we also find the transponder SRF to be again slightly less rotated than the

model. This could be due to a variety of issues including the following:

- the different processing used onboard ASCAT for calibration mode (e.g., the transponder alternates between two beams instead of all six, and the echo measurement windows are delayed to filter out the reflected signal from the Earth surface);
- the time delay used by the transponders before transmitting a return signal in response to an ASCAT signal, which may affect the Doppler velocity;
- the MetOp yaw steering law, which is not included in the SRF model;
- the rotation of the transponders as they track the satellite which may affect the Doppler velocity.

C. Features in NRCS Data

Finally, we examine actual ASCAT σ° data. Generally, the σ° values for land and vegetation are larger than for the open ocean. We select a study region that includes the island of Niue (19.06° S 169.87° W) in the Pacific Ocean. When the wind speeds are low, the large σ° values from the island provide an excellent contrast against the low σ° values of the surrounding ocean.

Due to the distributed nature of the SRF, measurements over the ocean but near Niue contain a combination of the true ocean σ° and the land σ° . Thus, some “blurring” in the σ° data is expected around the island. Due to the elliptical shape of the SRF, the blur is larger along one direction (oriented along the semimajor axis of the SRF ellipse) than along the perpendicular direction (oriented along the semiminor axis of the SRF ellipse). The blur is characterized by the land fraction and is discussed further in the following.

Niue is shown for geoprojected ASCAT backscatter in the upper left subfigure of Fig. 12. The GSHHG coastline² is overlaid on the σ° values. A few -3 dB contours of the measurement SRF are shown for scale and orientation. As expected, the σ° values near Niue are “blurred” in the orientation of the SRF semimajor axis.

To illustrate the significance of inaccuracies in the SRF estimate, a synthetic σ° scene is created for the Niue region, where land (the area within the Niue coastline) is set to -10 dB and ocean is set to -20 dB. The synthetic scene is sampled with three different SRF estimates: 1) a circular Gaussian with a -3 dB width of 25 km; 2) the estimate from [11] which assumes a rectangular shape perpendicular to the beam (i.e., $\alpha = 0$); and 3) the parameterization from Section IV. The sampled σ° values are shown in the remaining subfigures of Fig. 12 along with the SRF -3 dB contours for a few measurements. Of the three SRF types, only the estimate presented in this paper enables synthetic σ° measurements that match the observed values.

In all cases observed, the blurred backscatter matches the orientation of the SRF estimate, and we conclude that the parameterized SRF accurately models the characteristics of the ASCAT NRCS measurements.

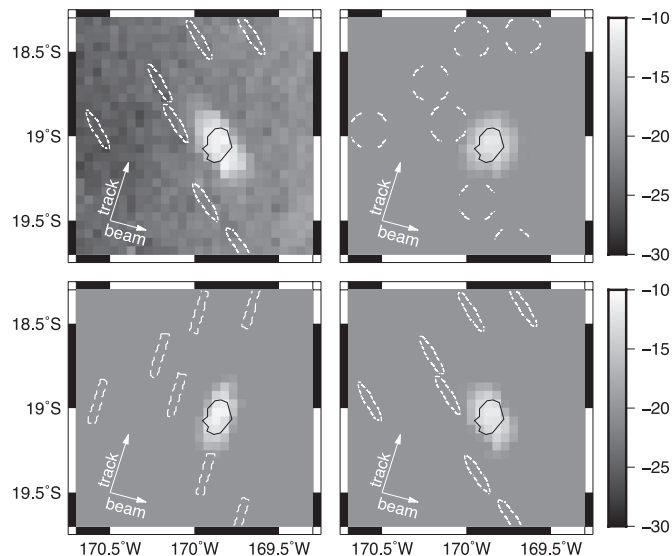


Fig. 12. ASCAT σ° measurements near Niue for the right mid beam on a grid spacing of 0.05° (≈ 6 km). The coastline of Niue is overlaid using a black line, and the SRF -3 dB contour for some measurements is indicated with white dashed lines. The top left subplot is the observed σ° measurements, and the remaining subplots are synthetic values sampled with different SRF estimates. (Top right) 25-km Gaussian SRF. (Bottom left) SRF that is perpendicular to the along-beam direction. (Bottom right) Parameterized SRF described in Section IV. For convenience, arrows indicate the along-beam and along-track directions.

VI. LAND FRACTION

Near-surface vector winds are retrieved from ASCAT measurements of ocean σ° values through inversion of a geophysical model function. Measurements near land may be corrupted or biased by nearby land σ° values due to the distributed spatial area of the SRF.

A distance-based metric may be used such that all ASCAT measurements within a certain distance from land (e.g., 30 km) are not used for wind retrieval. As the ASCAT measurement SRF is noncircular, many measurements may fall within the distance threshold but be oriented such that little or no land contamination is evident. This implies that a strictly distance-based threshold is overly conservative.

The LCR, or land fraction, is a valuable application of the SRF to ASCAT σ° data. As described in Section II, it characterizes the degree to which each measurement of σ° over the ocean is (possibly) contaminated by nearby land by incorporating information about the size, shape, and orientation of the measurement SRF. This information may be used for wind retrieval to reject or negatively weight measurements with high land contamination while keeping uncontaminated measurements [7]. This makes the LCR more useful for near-coastal wind retrieval than a distance threshold. The LCR is computed for each σ° measurement using (3) in conjunction with the SRF estimate and a high-resolution land map $L[x, y]$.

However, even if the SRF estimate is free from error, the LCR from (3) may not be exact since the land map may not accurately characterize coastal regions. The land map is a binary indicator of land or ocean, but for some coastal regions (e.g., marshes), the true σ° is not spatially homogeneous over the “land” portion, and the full integral formulation of the LCR from [7] is required. Notwithstanding this weakness, in practice, the LCR model is valid for most coastal regions.

²<http://www.soest.hawaii.edu/pwessel/gshhg/>

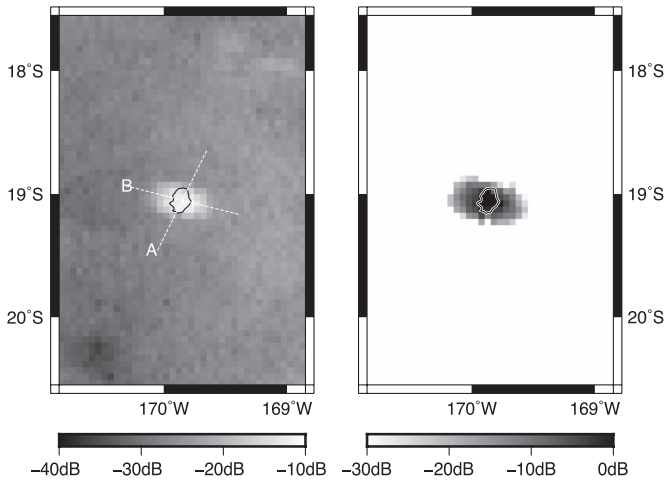


Fig. 13. Observed σ^0 (left) and computed LCR (right) near Niue on a grid spacing of 0.05° (≈ 6 km). The coastline is indicated with the solid line. The dashed lines are transects A and B for Fig. 14.

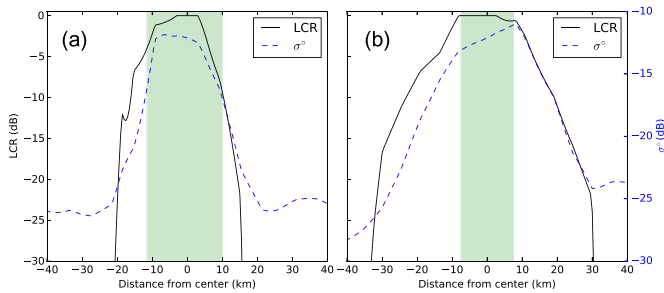


Fig. 14. Observed σ^0 and computed LCR values along transects A and B of Fig. 13. The horizontal axes correspond to moving along the transects, where positive values are toward northing (transect A) or easting (transect B). The portion of the transects over land is indicated with shading. The values between measurements are linearly interpolated.

The LCR is evaluated with σ^0 data for a region containing Niue in Fig. 13. The computed LCR compares well against the larger σ^0 values observed over Niue. As expected, the LCR shape and extent correspond to the “blurring” of σ^0 measurements around the island coast. Due to the SRF orientation and shape, the blur is not rotationally symmetric but spreads wider along one direction than another.

To examine the behavior of the LCR, Fig. 14 shows the interpolated LCR and σ^0 values along two transects over Niue, labeled A and B. The portions of the transects over land are also indicated in the figure. The number of LCR values above a threshold (e.g., -30 dB) differs for the two transects, indicating that the minimum land distance of uncontaminated measurements varies. Along transect A, the σ^0 measurements are only biased by land within about 5 km of land, representing a favorable SRF orientation. Transect B represents a worst-case SRF orientation, where the σ^0 measurements are land contaminated within about 25 km of land.

While a distance-based metric would uniformly discard all measurements within a distance threshold from land, using the LCR permits more measurements to be used in the direction of transect A than transect B. This reduces the retrievable coastal distance while still excluding land-contaminated σ^0 measurements.

VII. CONCLUSION

The ASCAT SRF is a quantity that characterizes the spatial extent and weighting of each ASCAT σ^0 measurement. We have modeled the SRF using the viewing geometry, antenna gain patterns, and details of the ASCAT onboard processing. We have also presented a computationally efficient SRF estimate that parameterizes the SRF based on measurement latitude and cross-swath position.

We have validated the estimated SRF by comparing it with the more accurate SRF model used during ground processing of ASCAT data. Minor differences exist between the SRF estimates, but for most SRF applications, these differences are negligible.

The estimated SRF is further validated through transponder data acquired periodically to calibrate ASCAT. The SRF agrees well with the transponder data, although we have observed a small rotation bias. This is primarily attributed to the differences in ASCAT onboard processing while in calibration mode versus normal measurement mode.

For future work, an additional SRF validation approach may more objectively characterize the accuracy of the parameterized SRF: the parameterized SRF may be used in the ASCAT ground processing at the PPF to estimate the σ^0 values from the raw measurement data. These σ^0 values may then be compared to the σ^0 estimates produced by the SRF presently used at the PPF. The distribution of the σ^0 errors may be used to quantify the accuracy of the SRF parameterization relative to the PPF SRF.

Another future improvement is to account for the yaw steering law of the MetOp satellite. As the attitude of MetOp varies, this, in turn, affects the Doppler shift on the ground, leading to small variations in the rotation of the SRF (the angle α as discussed previously). While this parameter has been unaccounted for, we expect that including it would only slightly modify the SRF estimate, since the validation results presented agree very well.

The SRF is useful for several applications of ASCAT σ^0 data, including estimating the land fraction of each measurement. The land fraction characterizes the degree to which a given σ^0 measurement may be affected by land. This is useful for near-coastal wind retrieval in order to flag or deweight σ^0 measurements before wind retrieval. For the cases examined, the computed land fraction agrees with the contaminated σ^0 values.

REFERENCES

- [1] R. D. Lindsley and D. G. Long, “Mapping surface oil extent from the Deepwater Horizon oil spill using ASCAT backscatter,” *IEEE Trans. Geosci. Remote Sens.*, vol. 50, no. 7, pp. 2534–2541, Jul. 2012.
- [2] W. Wagner *et al.*, “The ASCAT soil moisture product: A review of its specifications, validation results, and emerging applications,” *Meteorologische Zeitschrift*, vol. 22, no. 1, pp. 5–33, 2013.
- [3] M. P. Owen and D. G. Long, “Towards an improved wind and rain backscatter model for ASCAT,” in *Proc. IEEE IGARSS*, Jul. 2010, pp. 2531–2534.
- [4] J. Figa-Saldaña *et al.*, “The Advanced SCATterometer (ASCAT) on the Meteorological Operational (MetOp) platform: A follow on for European wind scatterometers,” *Can. J. Remote Sens.*, vol. 28, no. 3, pp. 404–412, 2002.
- [5] “Estimation of ASCAT-Normalised Radar Cross Section: ATBD,” EUMETSAT, Darmstadt, Germany, EUMETSAT ref. EUM/TSS/SPE/14/762689, Jul. 2014. [Online]. Available: ops@eumetsat.int

- [6] I. S. Ashcraft, "Projecting an Arbitrary Latitude and Longitude Onto a Tangent Plane," Brigham Young Univ., Microw. Earth Remote Sens. (MERS) Lab., Provo, UT, USA, Tech. Rep. 99-04, 1999. [Online]. Available: <http://www.mers.byu.edu/docs/reports/MERS9904.pdf>
- [7] M. P. Owen and D. G. Long, "Land-contamination compensation for QuikSCAT near-coastal wind retrieval," *IEEE Trans. Geosci. Remote Sens.*, vol. 47, no. 3, pp. 839–850, Mar. 2009.
- [8] R. D. Lindsley, "Estimating the ASCAT Spatial Response Function," Brigham Young Univ., Microw. Earth Remote Sens. (MERS) Lab., Provo, UT, USA, Tech. Rep. 14-01, May 2014. [Online]. Available: <http://www.mers.byu.edu/docs/reports/MERS1401.pdf>
- [9] C. Anderson, H. Bonekamp, C. Duff, J. Figa-Saldaña, and J. J. W. Wilson, "Analysis of ASCAT ocean backscatter measurement noise," *IEEE Trans. Geosci. Remote Sens.*, vol. 50, no. 7, pp. 2449–2457, Jul. 2012.
- [10] J. J. W. Wilson *et al.*, "Radiometric calibration of the advanced wind scatterometer radar ASCAT carried onboard the MetOp-A satellite," *IEEE Trans. Geosci. Remote Sens.*, vol. 48, no. 8, pp. 3236–3255, Aug. 2010.
- [11] R. D. Lindsley and D. G. Long, "Adapting the SIR algorithm to ASCAT," in *Proc. IEEE IGARSS*, 2010, pp. 3402–3405.



Richard D. Lindsley (S'08–M'16) received the Ph.D. degree in electrical engineering from Brigham Young University (BYU), Provo, UT, USA, in 2015.

From 2008 to 2015, he was with the Microwave Earth Remote Sensing Laboratory, BYU. He is currently with Remote Sensing Systems, Santa Rosa, CA, USA. His research interests include microwave remote sensing and signal processing.



Craig Anderson received the B.Sc. degree (Hons) in applied mathematics and the Ph.D. degree in theoretical solar physics from the University of St Andrews, Fife, U.K.

He worked for several years at the Marconi Research Centre, U.K., developing applications for airborne and spaceborne synthetic aperture radars before joining the European Organisation for the Exploitation of Meteorological Satellites (EUMETSAT), Darmstadt, Germany. For the last ten years, he has been involved in the calibration and validation

of the Advanced SCATterometer (ASCAT) instruments on the MetOp-A and MetOp-B satellites.



Julia Figa-Saldaña received the M.Sc. degree in civil engineering from the Universitat Politècnica de Catalunya, Barcelona, Spain, in 1993.

Since then, she has been involved in radar remote sensing processing and applications: first at the University Marine Engineering Laboratory and then with a Spanish Government Grant at the European Space Agency's Space Research and Technology Centre (ESA-ESTEC), working on applications of altimetry (1995–1996). This was followed by a European Organisation for the Exploitation of Meteorological Satellites (EUMETSAT), Darmstadt, Germany, research fellowship in the Royal Netherlands Meteorological Institute on scatterometry applications (1997–1999). After that, she joined EUMETSAT in 1999 and was involved in the specification and development of the Advanced SCATterometer (ASCAT) mission processing and cal/val, later on supporting the EUMETSAT Polar System and OSTM/Jason-2 operational processing. Since 2013, she has been leading a small team providing science and operational support to the EUMETSAT programs related to marine meteorology applications at EUMETSAT.



David G. Long (S'80–SM'98–F'08) received the Ph.D. degree in electrical engineering from the University of Southern California, Los Angeles, CA, USA, in 1989.

From 1983 to 1990, he worked for NASA's Jet Propulsion Laboratory (JPL), where he developed advanced radar remote sensing systems. While at JPL, he was the Project Engineer on the NASA Scatterometer (NSCAT) project which flew from 1996 to 1997. He also managed the SCANSAT project, the precursor to SeaWinds which was flown on QuikSCAT in 1999, on ADEOS-II in 2002, and on the International Space Station in 2014. He is currently a Professor with the Department of Electrical and Computer Engineering, Brigham Young University, Provo, UT, USA, where he teaches upper division and graduate courses in communications, microwave remote sensing, radar, and signal processing and is the Director of the BYU Center for Remote Sensing. He is the principal investigator of several NASA-sponsored research projects in remote sensing. He has over 400 publications in various areas including signal processing, radar scatterometry, and synthetic aperture radar. His research interests include microwave remote sensing, radar theory, space-based sensing, estimation theory, signal processing, and mesoscale atmospheric dynamics.

Dr. Long has received the NASA Certificate of Recognition several times and is an Associate Editor of the *IEEE GEOSCIENCE AND REMOTE SENSING LETTERS*.